Received: 24 April 2019 | Revised: 16 September 2019 | Accepted: 15 October 2019

DOI: 10.1002/we.2449

RESEARCH ARTICLE

WILEY

Aerodynamic loads on wind turbine nacelles under different inflow turbulence conditions

Jay Prakash Goit | Takeshi Ishihara

Department of Civil Engineering, The University of Tokyo, Tokyo, Japan

Correspondence
Jay Prakash Goit, Department of Civil Engineering, The University of Tokyo, 7-3-1 Hongo, Bunkyo-ku, Tokyo 113-8656, Japan.
Email: goitjay@gmail.com

Funding information
Development of Advanced Wind Power Technology Project funded by ClassNK, Hitachi, Ltd. and Shimizu Corporation

Abstract

The aerodynamic loads on wind turbine nacelles for range of inflow turbulence conditions are investigated. To this end, a series of wind tunnel experiments are conducted to investigate pressure field distributions over the surface of scaled models of rectangular and ellipsoidal nacelles. It is found that the mean pressure fields on the roof of the rectangular nacelle are similar for all the inflow turbulence cases for respective yaw angles. However, when yaw angle is around 90°, the mean pressure coefficient becomes more negative close to upstream edge with increasing inflow turbulence. For the ellipsoidal nacelle, the magnitude of the mean pressure coefficient increases with decreasing inflow turbulence in the adverse pressure gradient region, although the minimum peak pressure coefficient remains unaffected by inflow turbulence. The overall effect of wind-induced load on the nacelle surfaces is evaluated by computing force coefficients from the pressure data. It is observed that the peak force coefficients for both rectangular and ellipsoidal nacelles increase with increasing inflow turbulence. The models for the estimation of peak aerodynamic loads on the nacelle surfaces are proposed as functions of inflow turbulence and mean force coefficients and show satisfactory agreement with measurements. Finally, the loads calculated by the GL guideline are compared against the measurements. It is found that the guideline estimation is conservative for design load case (DLC) 6.1, but it underestimates the load by about 35% for DLC 6.2 when the inflow turbulence intensity is 13.2%.

KEYWORDS

aerodynamic load, coefficient of variation, inflow turbulence, peak factor, wind tunnel test, wind turbine nacelles

1 | INTRODUCTION

Aerodynamic forces, which are primarily associated with energy production from wind turbines, are also responsible for loading on turbine components. The loadings that arise during high wind speed or during extreme conditions like typhoons are called ultimate (or extreme) loads. Extreme loads are major concern during turbine design process. A large number of studies have investigated loads experienced by rotor blades, towers, and other major wind turbine components; most of the studies have used aeroelastic code such as FAST,[1-4] though investigation based on computational fluid dynamics (CFD), wind tunnel, and filed measurements are also plentiful.[5-7] However, wind turbine nacelle covers, which house drive trains, generators, control systems, etc. and are always exposed to the incoming wind, have not received same degree of attention. Although GL guideline,[8] which is widely accepted around the world for certification of wind turbine designs, have some specification dedicated to load

estimation on nacelle covers, International Electrotechnical Commission (IEC)[9] does not provide any information on nacelle cover design. Simple design of nacelle covers and lower cost compared with other major turbine components are salient factors responsible for reduced interest on load experienced by nacelle covers. However, nacelle damage in three out of six turbines in a wind farm was reported in the southern part of Japan during Typhoon Maemi, and the investigation by Ishihara et al[10] showed that the underestimation of the ultimate load during the design process was responsible for the damages. More recently in 2016, nacelle cover from one of the 600-kW wind turbines from Wajima wind farm,[11] Ishikawa, Japan, fell during extreme wind condition with peak value of 35.7 m/s. Similarly, nacelle covers and radiator covers of 14 out of 20 wind turbines from Minamiosumi wind farm,[12] Kagoshima, Japan, experienced partial or complete damage during typhoon No. 16 (MALAKAS) on 20 September 2016. The damages of nacelles during the typhoon and extreme wind are shown in Figure 1. Considering that nacelle covers house several important components of wind turbine and that their damage would lead to the shutdown of turbines, a thorough investigation of the aerodynamic loads acting on nacelle and proposition of methods for accurate estimation of such loads would be crucial. The current study analyses wind-induced loads on wind turbine nacelles through a series of wind tunnel experiments conducted for different inflow turbulence.

Nacelle designs of most utility-scale wind turbines can be considered as bluff bodies, and thus, flow and pressure distributions around those nacelles will have a lot of similarities to those around other bluff bodies, eg, buildings. Since there has been steady investigation on bluff body aerodynamics since past 50 to 60 years,[13] knowledge gained from those studies can certainly improve our understanding of nacelle aerodynamics. There is a large body of research focusing specifically on wind loading on low-rise buildings and structures.[14,15] The majority of those studies are based on pressure distributions obtained from wind tunnel tests or full-scale measurements. The measured pressure field can be integrated over the surface to estimate drag and cross-wind forces (eg, lift force). While the drag force is generally dominated by the difference in pressure between the front and back faces, the cross-wind force depends on flow separation and reattachment regions which generally have a negative pressure field. Such forces are responsible for unstable cross-wind motions of the structure (see, eg, Tamura and Kareem[16]) and unwanted loading on structures like nacelles. Fluctuating pressure data are also used in proper orthogonal decomposition (POD) to extract dominant features related to different force components.[17,18] Flow over nacelles can however show several evident differences when compared against other well-investigated bluff bodies. Aerodynamics interaction of nacelle with rotor and tower is the salient difference from other bluff body aerodynamics. Furthermore, ground effect with strong turbulence is crucial for, eg, low-rise building. Nacelles of utility-scale wind turbines, however, are installed on high towers, and thus, the ground effect has negligible impact.

As mentioned before, investigations of aerodynamic loads experienced by nacelle or the studies documenting reliability of existing design specifications are scarce. Noda and Ishihara[19] focused exclusively on aerodynamic forces on nacelles and conducted wind tunnel experiments to measure mean wind forces and local peak pressures. They obtained higher peak pressure coefficients from their experiments compared with those computed from GL guideline[8] specifications. In Goit et al,[20] the aerodynamic load on the top and side surfaces of a rectangular nacelle was investigated and a model for the estimation of nacelle loads was proposed. However, as the model is a function of yaw angle, it strongly depends upon the shape of the nacelle and cannot be sufficiently general. Furthermore, the measurements were conducted only for nonturbulent and very high turbulent inflow cases. Liu et al[21] investigated pressure distribution on a curved-shaped ellipsoidal nacelle for nonturbulent and highly turbulent inflow cases and also analyzed the effect of tower on pressure fields. Other studies have focused on accuracy of wind speed measured by nacelle-mounted anemometer and how that is affected by rotors and atmospheric turbulence (see, eg, Zahle and Sørensen[22] and Masson and Smaïli[23]), or they have investigated the thermal behavior of a wind turbine nacelle, taking into account wind speed, temperature, and the heat released by the electrical generator.[24]

The aim of this study is to investigate aerodynamic loads on rectangular and ellipsoidal wind turbine nacelles. The pressure fields on the nacelle surfaces are measured and compared for inflow turbulence of different levels. In order to investigate the overall effect of wind loads, aerodynamic forces are computed from the measured pressure data and are analyzed as the function of yaw misalignment and inflow turbulence. The measured data are then used to propose models for the accurate prediction of peak aerodynamic loads on nacelle surfaces, with the motivation that the models will act as a reference for developing standards related to nacelle design. Section 2 describes the wind tunnel setup, the scaled nacelle models, and the inflow characteristics. Results are presented and discussed in Section 3, where the pressure distribution and wind-induced forces for a range of inflows with different levels of turbulence are discussed. Models for peak wind load estimation are also proposed and discussed in this section. Finally, the main conclusions of this study are summarized in Section 4.

FIGURE 1 Damage to the nacelle cover during the typhoon at Minamiosumi wind farm[12] [Colour figure can be viewed at wileyonlinelibrary.com]

2 | MEASUREMENT SETUP AND FLOW CHARACTERIZATION

Measurements are conducted in a boundary layer wind tunnel at The University of Tokyo. It is a closed-circuit–type wind tunnel, and the test section is 11.8 m long, and has cross-section of 1.5 m x 1.8 m. A schematic of the test section setup is shown in Figure 2A. Turbulent boundary layers are generated by mean of spires, a fence, and blocks. Measurements are carried out for four different inflow profiles—one uniform inflow and three turbulent inflows with turbulence intensities of 4.0%, 9.5%, and 13.2%. Note that mean velocity at the hub height is maintained to 13.5 m/s for all four measurements. Spires and fences of different heights are installed to achieve the desired turbulence intensity at the nacelle position, which involve several trial-and-error iterations. Figure 2B shows the dimensions of the spires, fence, and blocks used to generate the inflow with the turbulence intensity of 13.2%. The dimensions of spires, fence, and blocks for all three cases of inflow turbulence are summarized in Table 1. It should be noted that a velocity as high as 13.5 m/s causes a severe sideways oscillation of the spires. Such oscillations are damped by installing a single horizontal bar of 0.02-m thickness along the tunnel width, fixed to all three spires.

Inflow profiles at the nacelle position are measured and characterized using a hot wire anemometer which is connected to a multichannel CTA (*Dantec 54N80*). Hot wire data are collected for the period of 1 minute for each height at 1-kHz sampling rate. The profiles are measured before nacelle model is installed in the test section. Figure 3 shows the vertical profiles of the normalized mean streamwise velocity u/u_h and turbulence intensity $I_u = \sigma/u$ for the uniform case and the three turbulence cases. Here, u_h and σ are the 1-minute average mean streamwise velocity and the standard deviation, respectively. It can be appreciated that the boundary layer height for the uniform flow normalized by the nacelle hub height z_h is around 0.3. Furthermore, it is found that the turbulence intensity for this case is 0.4% at the hub height level. The velocity profiles for all three turbulent cases roughly follows the power law profile given by:

$$u/u_h = (z/z_h)^{\alpha}. \tag{1}$$

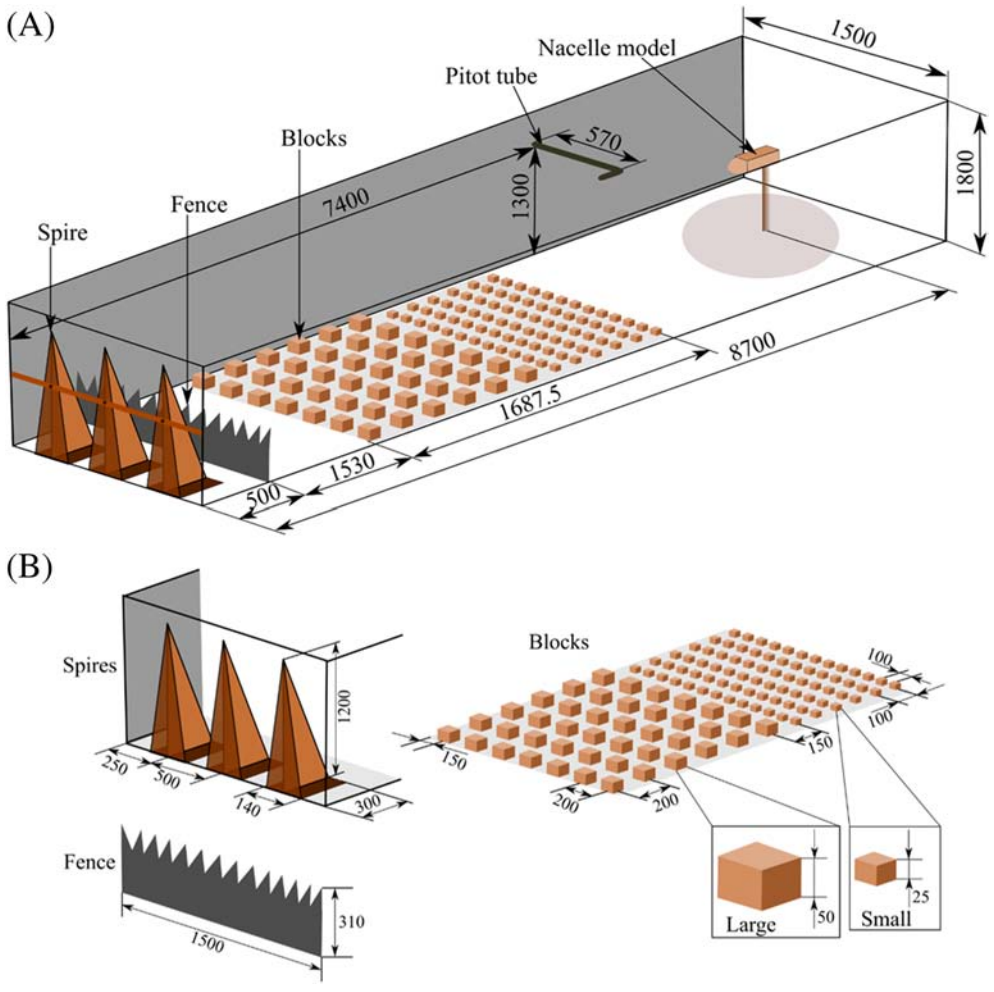

FIGURE 2 A, Schematic of wind tunnel test section depicting locations of spires, fence, blocks, and nacelle model. B, Dimensions of spires, fences, and blocks for I_u = 13.2% [Colour figure can be viewed at wileyonlinelibrary.com]

TABLE 1 Dimensions of spires, fences and blocks

	Turbulence level →	4%	9.5%	13.2%
Spires	Number	3	3	3
	Spacing between side spires and tunnel wall	250	250	250
	Spacing between spires	500	500	500
	Height	1200	1200	1200
	Streamwise × spanwise length at the base	300 × 90	300 × 140	300 × 140
Distance between spires and fence		N/A	500	500
Fence	Number	N/A	1	1
	Height		225	310
	Number of teeth		31	16
	Height of teeth		100	100
	Tooth spacing		50	100
Distance between fence and blocks		N/A	1530	1530
Large blocks	Streamwise × spanwise number of blocks	6 × 7	6 × 7	6 × 7
	Size	50	50	50
	Streamwise × spanwise spacing of blocks	200 × 200	200 × 200	200 × 200
Spacing between last row of large blocks and first row of small blocks		150	150	150
Small blocks	Streamwise × spanwise number of blocks	6 × 13	6 × 13	6 × 13
	Size	25	25	25
	Streamwise × spanwise spacing of blocks	100 × 100	100 × 100	100 × 100

Note. Lengths are in millimeters.

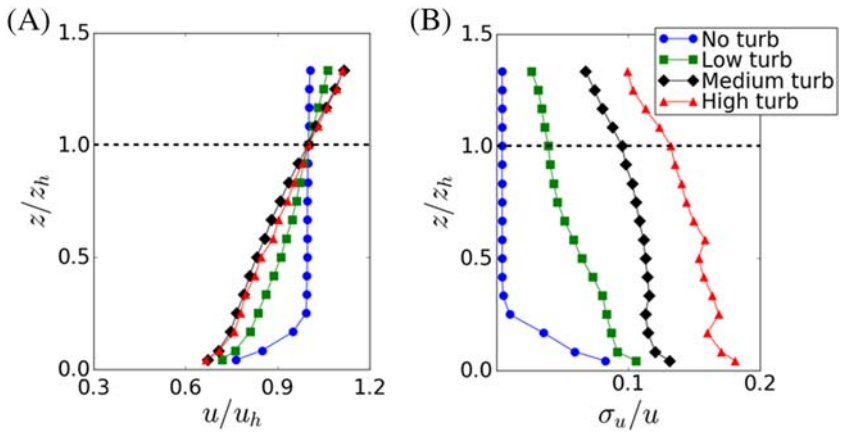

FIGURE 3 A, Mean velocity profiles and B, turbulence intensity profiles at the position of the nacelle model [Colour figure can be viewed at wileyonlinelibrary.com]

Figure 4 shows the rectangular and the ellipsoidal nacelle models used in the current study. The rectangular nacelle has dimensions of 200 mm × 80 mm × 80 mm, with an additional 80 mm for the hub, and it is mounted on a tower of height 560 mm. The ellipsoidal nacelle has a length of 200 mm and a width of 80 mm. The nacelle models are mounted to the turntable located at downstream side of the test section (cf Figure 2A). This would allow to vary the yaw angle with respect to incoming flow. The blockage ratios for both the nacelles—defined as the ratio of the nacelle frontal area to the test section cross-sectional area—are less than 1%, and therefore, its effect could be neglected in this study. Pressure data are collected using 92 pressure taps (84 on the top and eight on one side surface) for the rectangular nacelle and 160 pressure taps distributed on one side for the ellipsoidal nacelle (cf Figure 4). These pressure taps are connected to pressure transducers (Melon Technos Co, Ltd) with a range of ±1250 Pa and sensitivity of 125 Pa/V. 1.5 m-long tubes that have outer and inner diameters of 1.7 mm and 1 mm, respectively, are used to connect pressure taps from the nacelle surfaces to the transducers. Before the measurements, dynamic response of the tubes is investigated, and the phase and gain characteristics thus obtained are used to correct tubing related distortion of the pressure signals. Finally, the sampling frequency of the pressure measurement is set to 512 Hz.

Table 2 summarizes the experimental cases. As stated earlier, a uniform inflow is used for the first case, whereas for the other three cases, boundary layer profiles with different levels of turbulence intensities are used. Yaw angles were varied from 0° to 355° at intervals of 5°. Following Noda and Ishihara,[19] the counterclockwise direction with respect to the incoming flow is defined as a positive yaw angle. Although one data set of 64 seconds is enough to obtain stable mean pressure values for each yaw angle, the peak pressure values vary for different data sets even for the same yaw angle. This is due to fluctuating pressures. Therefore, five sets of data are collected for each yaw angle, and the maximum and minimum pressure coefficients for each yaw angle are calculated by averaging the peak pressure coefficients from all five data sets.[19]

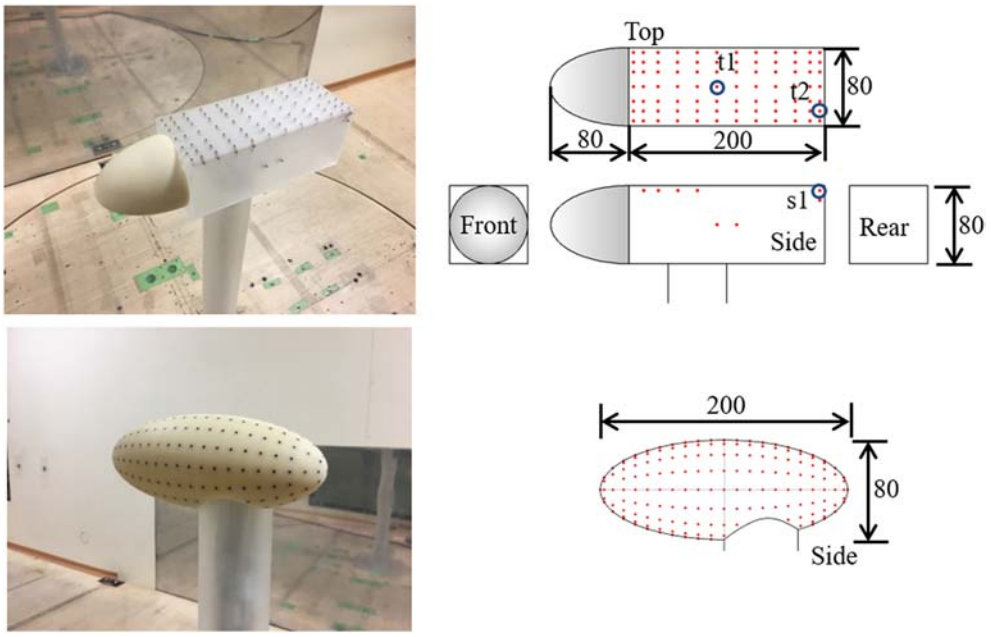

FIGURE 4 Rectangular nacelle (top) and ellipsoidal nacelle (bottom) models. Pressure orifices are predominantly distributed on the roof of the rectangular nacelle and on one side of the ellipsoidal nacelle [Colour figure can be viewed at wileyonlinelibrary.com]

TABLE 2 Measurement cases defined based on inflow turbulence

Case	Inflow Type	Hub Height Turbulence Intensity (I_u)	Yaw Angle (θ)
1	Uniform flow	0.4%	0° to 355° at 5° interval
2	Low turbulent shear flow	4%	
3	Medium turbulent shear flow	9.5%	
4	High turbulent shear flow	13.2%	

From the mean velocity at the hub height (u_h) of 13.5 m/s and using nacelle width which is 0.08 m, as a representative length, the Reynolds number will be 7.3×10^4. However, nacelles of a typical utility-scale wind turbine can roughly be 50 times larger than the nacelle models used in this study. Furthermore, wind speed during the extreme wind conditions can go as high as 50 m/s. Thus, the Reynolds number for full-scale nacelles exposed to actual extreme wind conditions can be higher than 3.5×10^6, which is 200 times that for current experiments. It may therefore be of an issue that the flow regime in the current study will be different from that for actual nacelles. However, it is commonly accepted in wind tunnel experiments of bluff bodies (eg, scaled-down model of buildings), that the edges and corners trigger separation, and the mechanism is similar regardless of the Reynolds number.[16] Note however that this reasoning may not be true for the ellipsoidal nacelle or even for the hub of the rectangular nacelle when it faces the incoming flow. Although this is the limitation of the scaled experiments, as it will be clear from the results, the peak loads occur during yawed conditions when the contribution of separation on the flow structure is dominant. Therefore, results from the current and other similar experimental works will not be of less importance. The parameter that is indeed important and is also the main subject of discussion in the current work is the inflow turbulence. As it will be clear from the following section, wind-induced force varies significantly with inflow turbulence. Since most onshore wind turbine installation sites have medium to high turbulence intensity depending upon the terrain complexity and most offshore sites have lower turbulence intensity, it is necessary to consider cases with low to high turbulence levels.

3 | RESULTS AND DISCUSSION

In this section, the pressure fields measured over the rectangular and ellipsoidal nacelle surfaces are first presented for uniform and turbulent inflows in Section 3.1. Wind-induced forces computed by integrating the pressure field are presented in Section 3.2. The effects of inflow turbulence and nacelle yaw angle on the measured pressure and aerodynamic loads are discussed. Finally, models for the estimation of the peak aerodynamic loads experienced by nacelles is proposed based on the measured data and is illustrated in Section 3.3.

3.1 | Pressure field distribution

Pressure data collected for the inflow cases and yaw directions mentioned in Table 2 can compute pressure coefficients given by

$$C_{p,i} = \frac{(p_i - p_{\text{ref}})}{1/2\rho u_h^2}, \tag{2}$$

where p_i is the instantaneous pressure, i is the pressure tap number, and p_{ref} is the reference static pressure.

In Figure 5, the variations of the pressure coefficients as a function of the yaw angle are shown for the rectangular nacelle, for a few selected points (cf Figure 4) for case 4 with 13.2% turbulence intensity. For the validation of the current experiment campaign, the results are compared against earlier measurements by Noda and Ishihara.[19] It can be appreciated that the results from the two measurement campaigns agree well, even though the experiments were conducted in different wind tunnels and with different setups. For point t1, which is at the center of the top surface, the minimum values of both mean pressure coefficient ($C_{p,\text{mean}}$) and the minimum peak pressure coefficient ($C_{p,\text{min}}$) are observed in two yaw angle ranges, i.e., $50° \leq \theta \leq 120°$ and $230° \leq \theta \leq 310°$. However, point t2, located near the edge of the top surface, experiences a strong negative pressure for a range of yaw angles, and the minimum pressure coefficient is observed around 210°. This large negative pressure observed for point t2 is due to the fact that the effect of separation is more pronounced for the points at the edge. Point s1, located on the side surface, faces the incoming flow for the yaw angle range $180° \leq \theta \leq 360°$. Therefore, $C_{p,\text{max}}$ is close to or larger than zero in this yaw angle range, and the maximum peak pressure ($C_{p,\text{max}}$) is observed at 235°.

Figure 6 shows the mean pressure coefficient field for the uniform flow case and for all three turbulent boundary layer cases for yaw angles 0°, 15°, and 90° for the rectangular nacelle. Results for 15° yaw angle are shown in the figure because IEC standard considers yaw misalignment of ±15° when computing loads for the design load case (DLC) 6.1, which corresponds to the parked condition of wind turbine during extreme wind condition and without grid loss.[9] It can be appreciated that for all four inflow cases and for all the yaw misalignments, the mean pressure coefficients ($C_{p,\text{mean}}$) are either negative or close to 0. Because the sharp edge of one of the sides of the nacelle facing the incoming flow increases when the yaw angle increases from 0° to 90°, the region on the nacelle surface with negative $C_{p,\text{mean}}$ also increases. This is because the sharp edge is responsible for flow separation which consequently increases the area with negative pressure coefficients. When the yaw angle is 0°, the hub faces the incoming flow; the curved shape of the hub greatly streamlines the flow and reduces the flow separation region on the nacelle. Furthermore, it can be observed that for 0°, distribution of the $C_{p,\text{mean}}$ for all four inflow cases are similar. However, differences between pressure fields

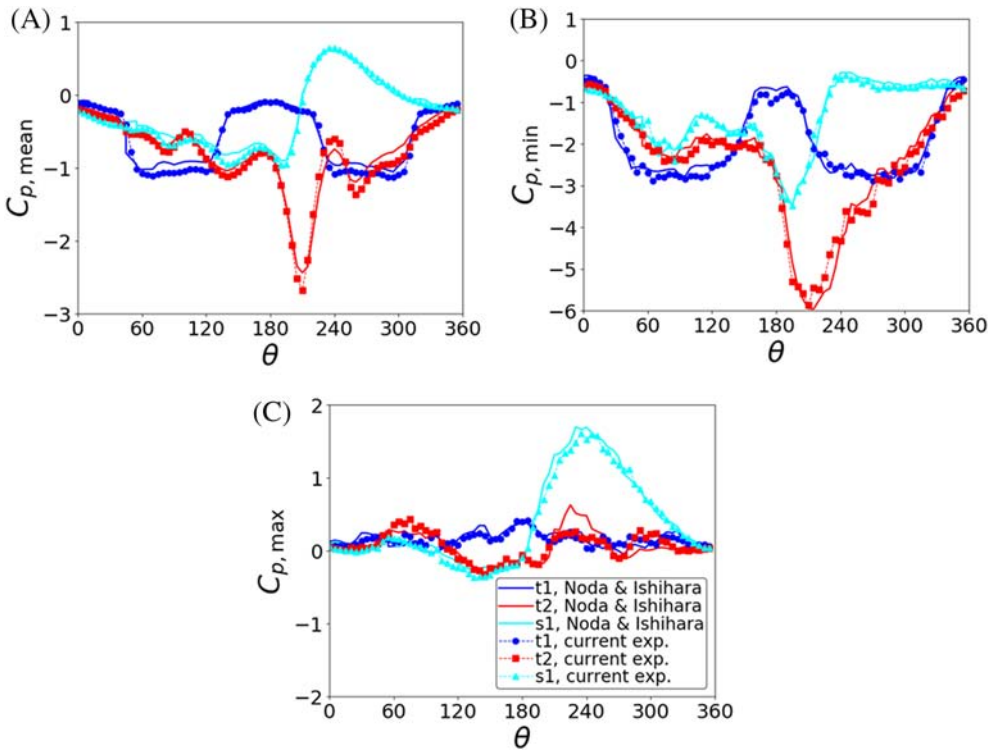

FIGURE 5 Variation of pressure coefficients as a function of yaw angle for the rectangular nacelle for the case of high turbulent shear inflow (I_u = 13.2%). Results from current experiments are compared against measurements by Noda and Ishihara.[19] A, Mean pressure coefficients, B, minimum peak pressure coefficients, C, maximum peak pressure coefficients [Colour figure can be viewed at wileyonlinelibrary.com]

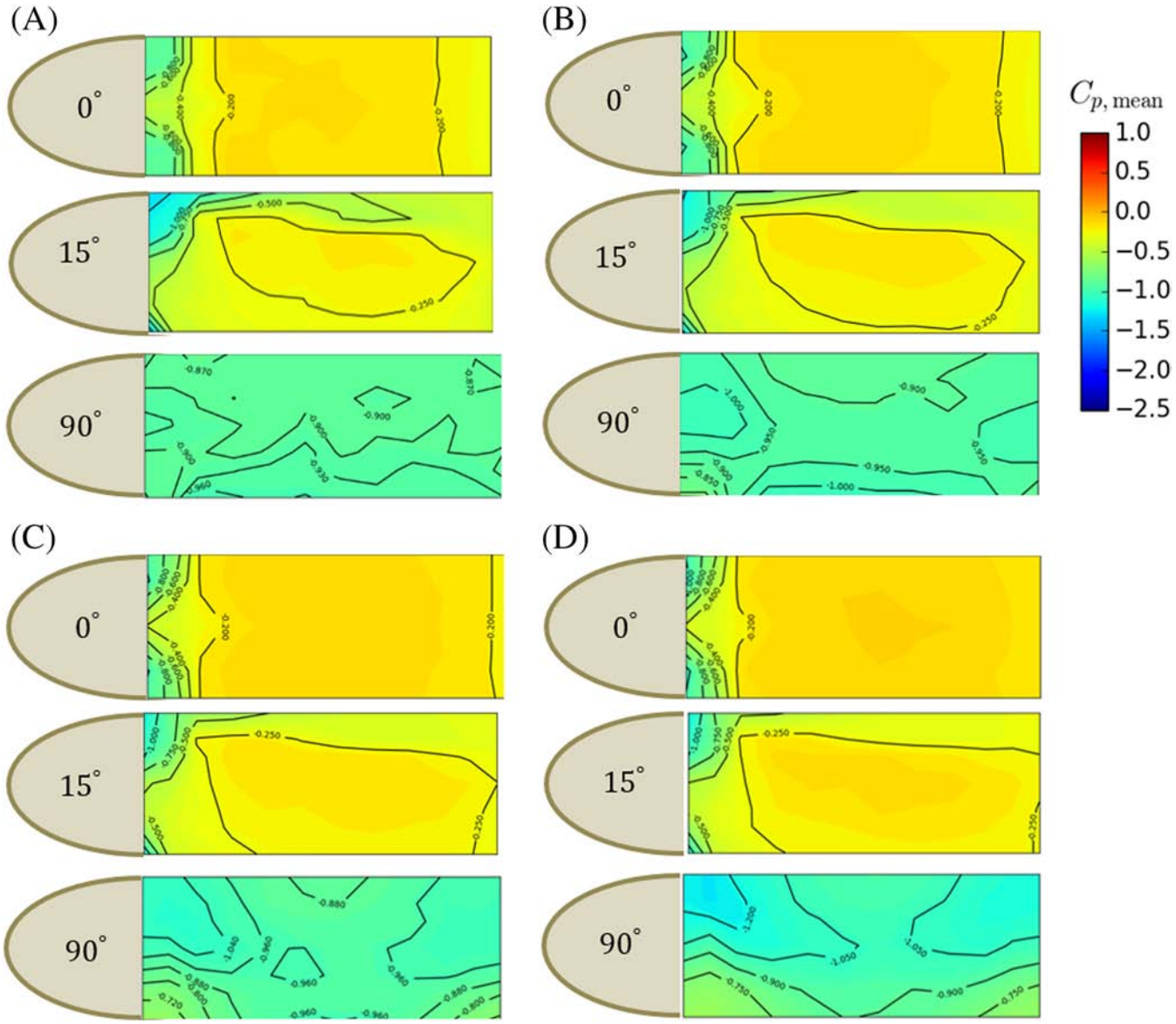

FIGURE 6 Time-averaged field of pressure coefficient on the top surface of the rectangular nacelle. A, Uniform inflow, B, Low turbulent shear inflow, C, Medium turbulent shear inflow, D, High turbulent shear inflow [Colour figure can be viewed at wileyonlinelibrary.com]

for different inflow cases become more significant with increasing yaw misalignment. For the yaw angle of 90°, $C_{p,\text{mean}}$ becomes more negative close to the upstream edge with increasing inflow turbulence. However, at the same time the downstream extent of the negative pressure region reduces with increasing inflow turbulence. Although the mechanism behind this phenomenon is not explored in the current study, one logical speculation can be that strong inflow turbulence is responsible for increased maximum wind speed which entrains high speed flow towards the nacelle surface and thus enhances the separation bubble.

Figure 7 presents contours of the mean pressure coefficient for the uniform case and for the turbulent boundary layer case with a turbulence intensity of 13.2%, for yaw angles 0°, 45°, 135°, 180°, and 270° for the ellipsoidal nacelle. For yaw angles 0° and 180°, a positive pressure field can be observed in the region facing the wind and upstream of the tower. However, further downstream, an adverse pressure gradient results in a negative pressure field with a minimum $C_{p,\text{mean}}$ as low as −1.0 for the uniform case and −0.6 for the turbulent boundary layer case. The magnitude of the minimum $C_{p,\text{mean}}$ is the lowest behind the tower. It can also be appreciated that the effect of the tower is more dominant for the uniform inflow case than for the turbulent cases. For yaw angles 45° or 135°, the side of the nacelle surface with pressure taps are on the downwind side relative to the incoming flow, and thus, it is in the negative pressure region. The minimum $C_{p,\text{mean}}$ can be observed around the edge of the displayed surface, with a peak value of approximately −1.5 for the uniform inflow case and −1.2 for the turbulent boundary layer case. For the yaw angle of 270°, the side with the pressure taps displayed in the figure faces the incoming flow. Consequently, a large region with positive $C_{p,\text{mean}}$ is observed for both the uniform and turbulent inflow cases.

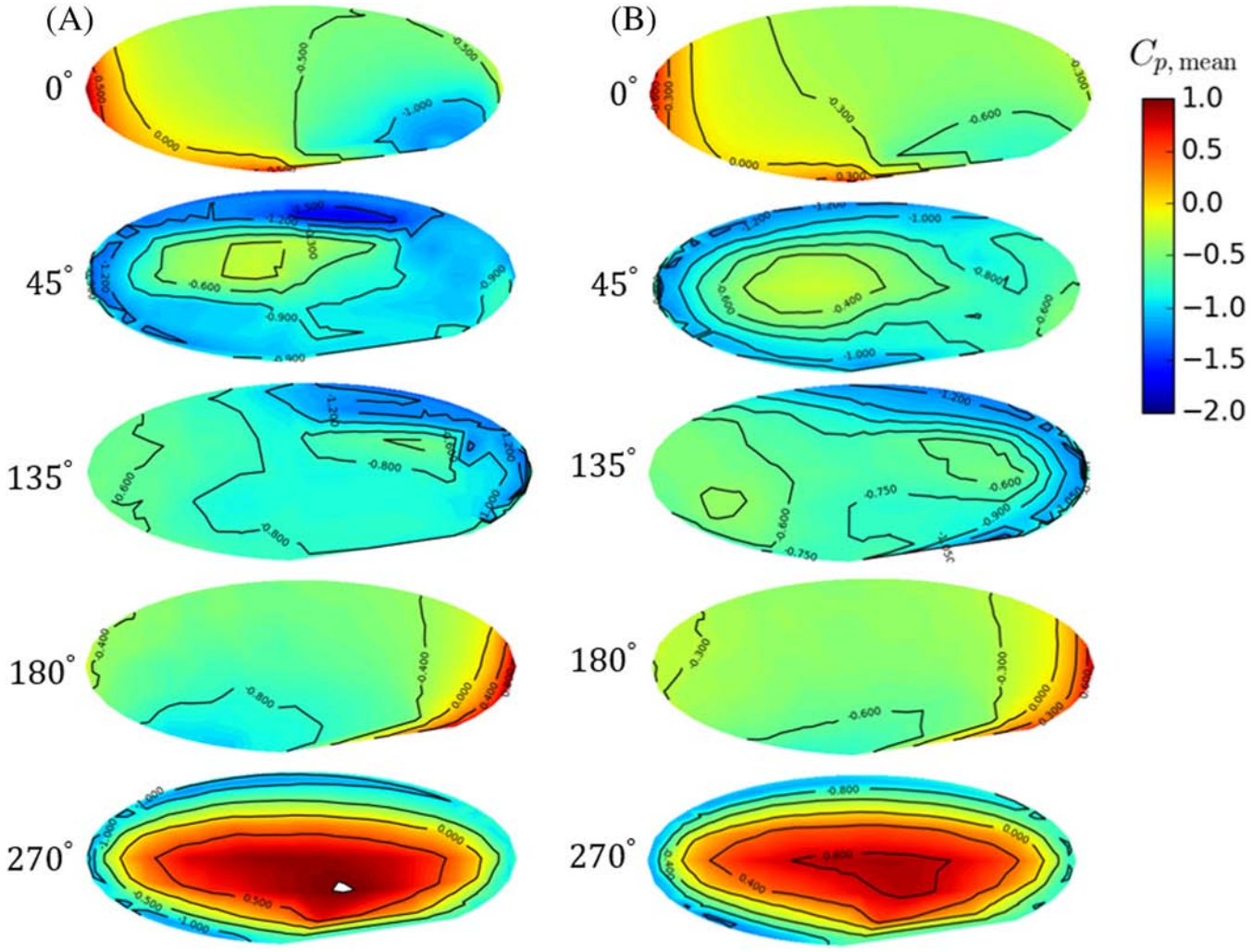

FIGURE 7 Time-averaged field of pressure coefficient on the side surface of the ellipsoidal nacelle for 0°, 45°, 135°, 180°, and 270° yaw angles. A, Uniform inflow, B, High turbulent shear inflow [Colour figure can be viewed at wileyonlinelibrary.com]

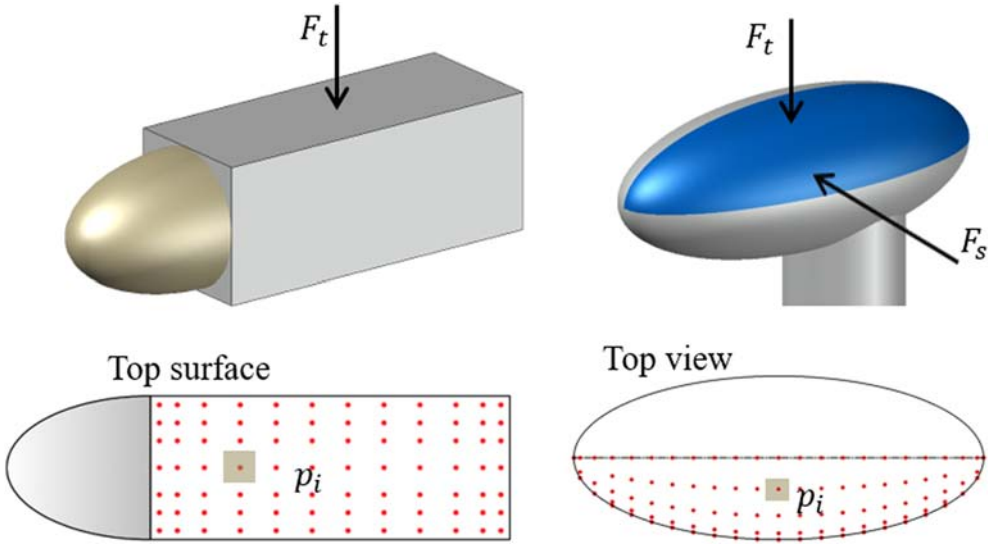

FIGURE 8 Schematic showing the definitions of the forces on the nacelle surfaces [Colour figure can be viewed at wileyonlinelibrary.com]

3.2 | Aerodynamic loads on nacelles

The measured pressure fields are next used to compute total wind-induced forces acting on the nacelle. For the rectangular nacelle, the vertical components of forces normal to the top surface are investigated, while for the ellipsoidal nacelle, vertical and sideways forces on half of the upper surface are investigated (cf Figure 8). The force for the rectangular nacelle corresponds to the opening of the nacelle cover from one side and those for the ellipsoidal nacelle correspond to the nacelle opening from the middle. The forces are computed by integrating pressure field over the nacelle surface, and the vertical force on the top surface of the rectangular nacelle is given by

$$F_{\mathrm{t}} = -\int_A p \mathrm{d}A \quad = -\sum_{i=1}^{N} p_i \mathrm{d}A_i, \tag{3}$$

where $\mathrm{d}A_i$ is the differential area around the pressure tap *i*. F_{t} is a lift force acting on the nacelle roof, and it has possible damaging effect compared with the drag force, which can be neglected. For the ellipsoidal nacelle, the vertical and sideways components of the point-wise pressure need to be integrated.

$$\begin{aligned} F_{\mathrm{t}} &= -\int_A p_t \ \mathrm{d}A \quad = -\sum_{i=1}^{N} p_{i,t} \ \mathrm{d}A_i \\ F_{\mathrm{s}} &= -\int_A p_s \ \mathrm{d}A \quad = -\sum_{i=1}^{N} p_{i,s} \ \mathrm{d}A_i \end{aligned} \tag{4}$$

Here, $\boldsymbol{p_t}$ and $\boldsymbol{p_s}$ are the vertical and sideways components of the pressure. The coefficients of the vertical and sideways forces are then given by

$$\begin{aligned} C_{F,\mathrm{t}} &= \frac{F_{\mathrm{t}}}{1/2\rho u_{\mathrm{h}}^2 A} \\ C_{F,\mathrm{s}} &= \frac{F_{\mathrm{s}}}{1/2\rho u_{\mathrm{h}}^2 A} \end{aligned} \tag{5}$$

where *A* is the total surface area.

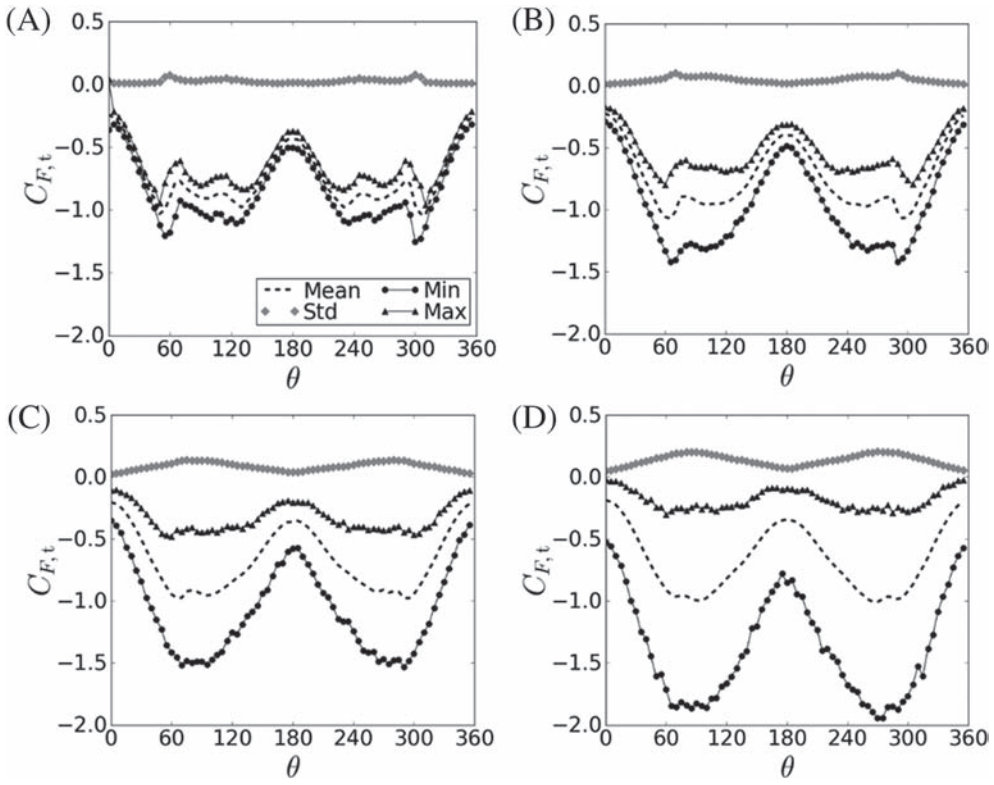

FIGURE 9 Force coefficients on the top surface of the rectangular nacelle. A, Uniform inflow (I_{u} = 0.4%), B, Low turbulent shear inflow (I_{u} = 4.0%), C, Medium turbulent shear inflow (I_{u} = 9.5%), D, High turbulent shear inflow (I_{u} = 13.2%)

Figure 9 shows the vertical force coefficients on the top surface of the rectangular nacelle as a function of yaw angle, for the uniform inflow case and the three turbulence cases. It can be observed that the mean, maximum, and minimum force coefficients are negative, i.e., outward from the nacelle surface (cf Figure 8 for the definition of the direction of forces), for all yaw angles. The reason is that pressure coefficients on the top surface of the rectangular nacelle are negative for all the yaw angles. For the uniform inflow case, the peaks of the minimum and mean $C_{F,t}$ are at 60° and 300°, although for yaw angles between 45° and 135° and yaw angles between 225° and 315°, the variation in $C_{F,t}$ is minimal. Furthermore, the difference between the maximum, minimum, and mean force coefficients is not too large. On the other hand, the difference between the mean and minimum $C_{F,t}$ increases with inflow turbulence and becomes significantly large for the high turbulence case. The peaks of minimum and mean $C_{F,t}$ also become more distinct with increasing inflow turbulence. For the high turbulence case, those peaks are observed around 90° and 270°. Compared with the uniform inflow case, the magnitudes of the minimum force coefficient and standard deviation are larger for the turbulence inflow cases. It is clear from the above results that the level of turbulence intensity in the incoming flow plays important role in nacelle aerodynamics, and in particular, peak load acting on the nacelle surface increases with increasing turbulence level. Therefore, the site-specific turbulence intensity may be an important parameter to be considered during nacelle design process.

Figure 10 shows the variation of the mean, minimum, and maximum vertical force coefficients and the standard deviation on the ellipsoidal nacelle, for the uniform inflow case, and the high turbulence case. As shown in the case with the rectangular nacelle, the mean, maximum, and minimum vertical force coefficients are negative for all yaw angles. As the yaw angle increases, the vertical force coefficient increases for both the uniform and turbulent inflow cases. The peaks of the mean and minimum force coefficients are observed at θ = 60° for both cases. The peak minimum $C_{F,t}$ for the uniform inflow is around −1.0 while that for the turbulence shear flow is −1.45. The differences between the mean, maximum, and minimum $C_{F,t}$ are not too large for the uniform inflow case, and the magnitudes of the standard deviation are smaller compared with the turbulence inflow case. Figure 11 shows the sideway force coefficients. The mean and minimum force coefficients are again negative for most yaw angles and for both the uniform and turbulent inflow cases. However, the maximum $C_{F,s}$ is positive for yaw angles between 270° and 290° for the uniform inflow case and for yaw angles between 205° and 340° for the high turbulence case. The positive $C_{F,s}$ can be attributed to the fact that a large portion of the nacelle faces the incoming flow for these yaw angle ranges.

3.3 | Models for peak aerodynamic load estimation

It is clear from the results presented in Section 3.2 that the aerodynamic load experienced by wind turbine nacelles depends on the inflow turbulence (increases with increasing turbulence intensity), the yaw angle which is the misalignment between the wind and yaw direction, and the shape of the nacelle. Models for the estimation of the peak aerodynamic load experienced by nacelles is proposed in this section. The model-estimated peak loads are also compared against loads estimated using the pressure coefficients specified by the GL guideline.[8]

The proposed model follows the quasi-steady assumption which is well accepted in wind engineering.[25] Following this assumption, wind-induced peak force coefficient $\widehat{C}_F$ can be expressed in terms of mean force coefficient $\overline{C}_F$ and two additional terms called peak factor (g) and coefficient of variation (I_{C_F}):

$$\widehat{C}_F = (1 + g I_{C_F})\overline{C}_F. \tag{6}$$

Here, g and I_{C_F} are defined as

$$g = \left|\frac{\left(\widehat{C}_F - \overline{C}_F\right)}{\sigma_{C_F}}\right|, \qquad I_{C_F} = \left|\frac{\sigma_{C_F}}{\overline{C}_F}\right|, \tag{7}$$

where σ_{C_F} is the standard deviation of the force coefficient. The common practice in wind engineering is to use g = 3.5 and $I_{C_F} = 2I_u$. However, the measured results show that g, which is the difference between the peak and mean force coefficients, cannot have a constant value and is a

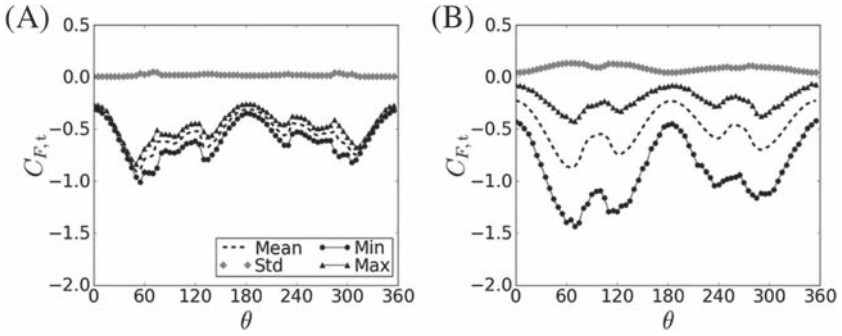

FIGURE 10 Vertical force coefficients on the ellipsoidal nacelle. A, Uniform inflow (I_u = 0.4%), B, High turbulent shear inflow (I_u = 13.2%)

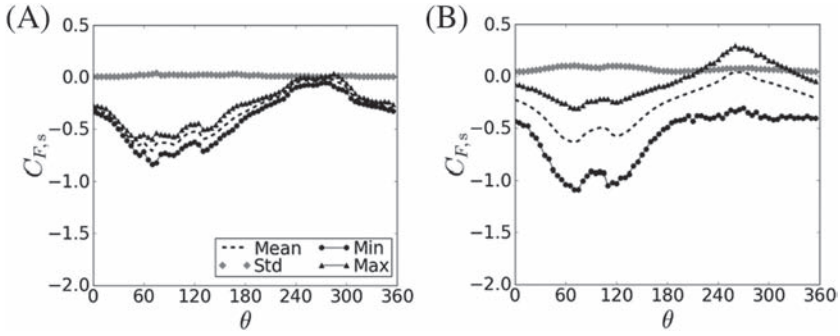

FIGURE 11 Sideway force coefficients on the ellipsoidal nacelle. A, Uniform inflow (I_u = 0.4%), B, High turbulent shear inflow (I_u = 13.2%)

function of inflow turbulence as well as of yaw angle (cf Figures 9–11). Similarly, the coefficient of variation (I_{C_F}) varies with the yaw angle. Therefore, for the accurate prediction of the peak aerodynamic load, it is necessary to propose new models that take these factors into account. It should be noted, however, that any such models, which are a function of yaw angle, cannot be general, since the yaw angle dependence of the peak force is dictated by the shape of the nacelle. Thus, the following models for g and I_{C_F} as a function of the mean force coefficient $\overline{C}_F$ and inflow turbulence intensity I_u are proposed:

$$\begin{aligned} g &= f(\overline{C}_F, I_u) = a\tan^{-1}(2\overline{C}_F + 1) + b \qquad \text{for } \overline{C}_F < 0, \\ I_{C_F} &= f(\overline{C}_F, I_u) = c\tan^{-1}(2\overline{C}_F + 1) + d \qquad \text{for } \overline{C}_F < 0, \\ a &= 16 I_u k, \quad b = 18 I_u k + 3.6, \quad c = 0.3 I_u k, \quad d = 1.8 I_u k, \\ k &= \begin{cases} 1.0 \text{ for rectangular nacelle} \\ 0.8 \text{ for ellipsoidal nacelle} \end{cases} \end{aligned} \tag{8}$$

Figure 12 shows the measured and model-estimated values of the peak factor (g) and coefficient of variation (I_{C_F}) as a function of the mean force coefficient ($\overline{C}_F$) for the vertical force on the roof of the rectangular nacelle. The models are developed from the fit to the g and the I_{C_F} obtained from the measurements. Note that for the rectangular nacelle, the pressure taps are predominantly distributed on the nacelle roof, and thus, the forces on the nacelle roof could only be computed. Since both the mean and peak force coefficients on the nacelle roof are negative,

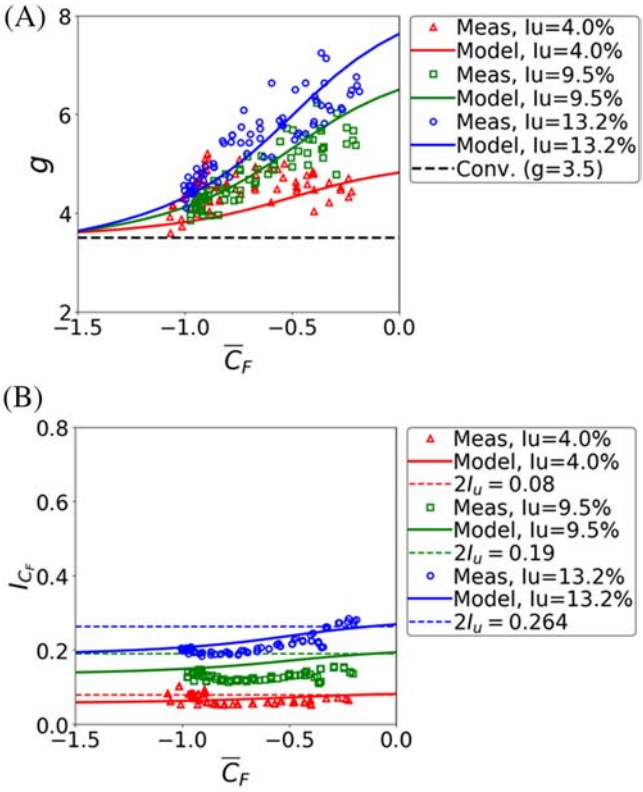

FIGURE 12 Measured values and model-estimated values of (A) Peak factor (g) and (B) coefficient of variation (I_{CF}) for turbulence intensities of 13.2%, 9.5%, and 4.0% for the rectangular nacelle. Conventionally accepted values of g and I_{CF} are also plotted[25] [Colour figure can be viewed at wileyonlinelibrary.com]

g and I_{C_F} cannot be evaluated for positive $\overline{C}_F$. It can be seen from the figure that the values of g and I_{C_F} obtained from the measurement are dependent on $\overline{C}_F$. It is interesting to find that the lower limit for g is 3.5, i.e., the same as the conventionally accepted value. The peak factor converges to this limiting value for all three turbulent inflow cases. However, the value of g increases significantly when the magnitude of the negative $\overline{C}_F$ decreases. g also increases with the inflow turbulence. Therefore, it can be concluded that g cannot have a single constant value and that it should be a function of $\overline{C}_F$ and inflow turbulence as proposed in the model in Equation (8). Although the variation of g and I_{C_F} for positive $\overline{C}_F$ could not be computed from the current setup, from the measurement data of Noda and Ishihara,[19] it is found that g does not vary much and is close to 3.5 for all positive $\overline{C}_F$. Therefore, it is not necessary to propose any new model for that. Regarding I_{C_F} for positive $\overline{C}_F$, it slightly varies with the mean force coefficient and may be approximated by the conventional model, $I_{C_F} = 2I_u$. The proposed models for g and I_{C_F} also show acceptable agreement with the measured data for the ellipsoidal nacelle, and this will be clear from the following comparisons.

Figure 13 compares the peak vertical force coefficients on the top of the rectangular nacelle and the upper half of the ellipsoidal nacelle estimated using the proposed models (cf Equation 8) against the measured values. Note that since the vertical force is negative for the entire yaw angle range, the peak force coefficients are always minimum force coefficients in this study. The model-predicted peak forces show good agreement with the measured values for both rectangular and ellipsoidal nacelles. Although the model is built largely by fitting to the rectangular nacelle data, the agreement is acceptable for the ellipsoidal nacelle as well. For the ellipsoidal nacelle, the model slightly overestimates the magnitude of the force coefficient. This will still allow a conservative design of the nacelle with the proposed models. A large number of utility-scale wind turbines have a nacelle with an intermediate design between the two extreme models considered in this study. Most nacelles are rectangular with curved edges. The peak force coefficients estimated using pressure coefficients specified by the GL guideline[8] are also shown in Figure 13A,C. The pressure coefficient on the roof of nacelles with sharp edge like the rectangular nacelle is specified to be −0.6 in the GL guideline. For rounded shaped nacelle like the ellipsoidal nacelle, the GL guideline states that the $\overline{C}_p$ can be reduced by 20%. With the $\overline{C}_p$ values known, the mean pressure ($\overline{p}$) and force ($\overline{F}$) can be calculated using

$$\overline{p} = 1/2\rho u_h^2 \overline{C}_p,\ \overline{F} = \overline{p}A = 1/2\rho u_h^2 C_p A. \tag{9}$$

The mean and peak force coefficients can then be estimated using the following relations:

$$\overline{C}_F = \frac{\overline{F}}{1/2\rho u_h^2 A},\ \widehat{C}_F = G^2 \overline{C}_F, \tag{10}$$

where G is the gust factor with a commonly accepted value of 1.4. The peak force computed using GL guideline specification underestimates the magnitude of peak force coefficient for a large range of yaw angles. For the high turbulence case, the GL guideline underestimate the maximum peak force coefficient by more than 40% for both nacelles.

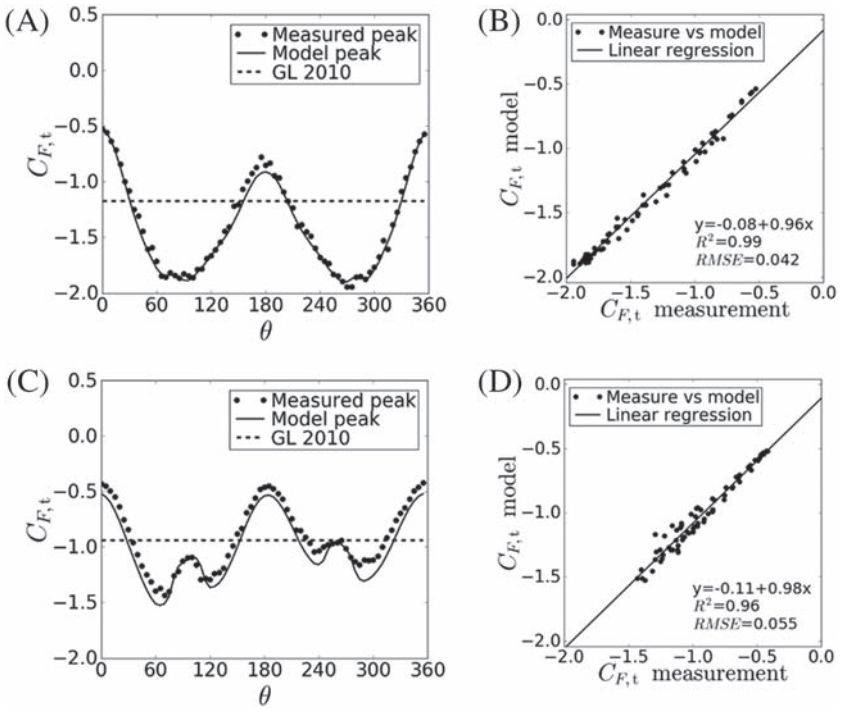

FIGURE 13 Comparison between predicted and measured peak force coefficients for inflow turbulence intensity 13.2%. A and B, Vertical force on the roof of rectangular nacelle. C and D, Vertical force on the upper half of the ellipsoidal nacelle

TABLE 3 Comparison between predicted and measured peak force coefficients

Nacelle Type	Inflow Turbulence	Slope (m)	Offset (c)	R^2
Rectangular (vertical force)	4%	0.86	−0.11	0.98
	9.5%	0.97	−0.13	0.99
	13.2%	0.96	−0.08	0.99
Ellipsoidal (vertical force)	4%	0.94	−0.03	0.96
	9.5%	1.01	−0.08	0.96
	13.2%	0.98	−0.11	0.96

Scatter plots of the comparisons for the high turbulence case are also shown in Figure 13. For the rectangular nacelle, the coefficient of determination (R^2) is 0.99, thus showing a very high correlation between the measured and model-predicted values. For the ellipsoidal nacelle, R^2 is 0.96. A comparison of the model-predicted and measured peak force coefficients for all three turbulence cases and both nacelle types are summarized in Table 3.

The above comparisons show that peak aerodynamic loads on nacelles can be estimated with acceptable accuracy using the models proposed in the current study. However, Equations (6) and (8) still require mean force coefficient ($\overline{C}_F$). The $\overline{C}_F$ can be computed from the integration of mean pressure coefficient ($\overline{C}_p$) over the surface. It is clear from the pressure field distribution presented in Section 3.1 that $\overline{C}_p$ varies even over a surface and that the GL guideline specified constant $\overline{C}_p$ value for each surface is not realistic. Therefore, the mean pressure coefficient distributions are proposed based on the measured pressure data (cf Figures 6 and 7). The proposed $\overline{C}_p$ distribution is then used to estimate $\overline{C}_F$ for models in Equations (6) and (8). Figure 14 shows the proposed mean pressure distribution for DLC 6.1 (i.e., yaw misalignment range of ±15°) and for DLC 6.2 (i.e., yaw misalignment range of ±180°) for the top surfaces of the rectangular and ellipsoidal nacelles. Note that in Figure 14, L and W stand for the length and width of the nacelle.

Figure 15 shows the peak force coefficient computed from the proposed model—and the pressure distributions in Figure 14—as the function for turbulence intensity. It can be appreciated that the model-estimated values are in good agreement with the measurements for both rectangular and ellipsoidal nacelles. Furthermore, the models are successfully able to account for the effect of inflow turbulence which is crucial in deciding the magnitude of wind-induced loads. Finally, the magnitude of $\widehat{C}_{F,t}$ predicted by the GL guideline is larger than the measurements, and the values are conservative for DLC 6.1. However, for DLC 6.2, the magnitude of $\widehat{C}_{F,t}$ predicted by the GL guideline is lower for the turbulence cases. For the high turbulence case, the GL-predicted value is about 35% lower than the measurement for both rectangular and ellipsoidal nacelles.

Note that the current study focused on the external pressure and did not measure internal pressure. However, since the wind-induced load acting on the nacelle covers results from the difference in the external and internal pressures, the latter will also be important during the nacelle design. The method for estimating peak pressure coefficients on the nacelle covers from the external and internal pressures is discussed in the JSCE guideline (see Ishihara[26]). This guideline has proposed following relation for computing peak pressure coefficient ($\widehat{C}_p$):

$$\widehat{C}_p = \widehat{C}_{pe} - C_{pi}, \tag{11}$$

where $\widehat{C}_{pe}$ is the peak external pressure coefficient and C_{pi} is the coefficient representing the effect of the variation in the internal pressure. The values of C_{pi} specified in the JSCE guideline for positive and negative $\widehat{C}_{pe}$ values are

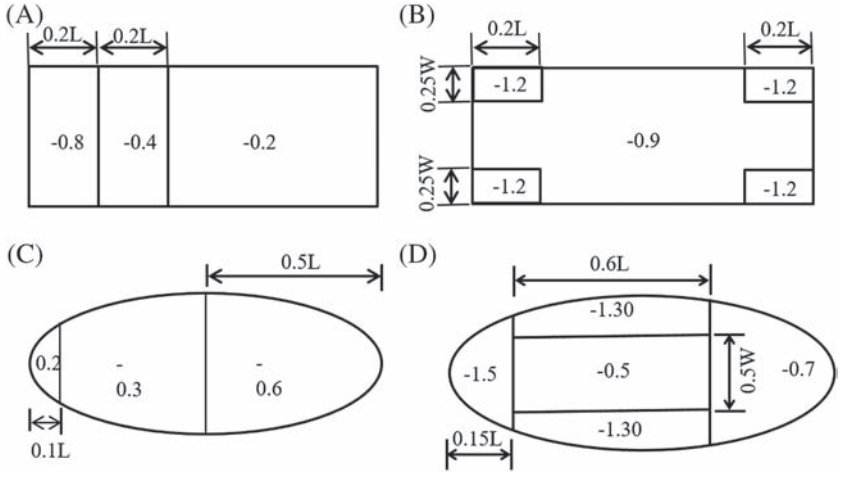

FIGURE 14 Proposed mean pressure coefficient distribution. A and B, Top surface of rectangular nacelle, C and D, Top view of ellipsoidal nacelle. (A) and (C): for design load case (DLC) 6.1; (B) and (D): for DLC 6.2

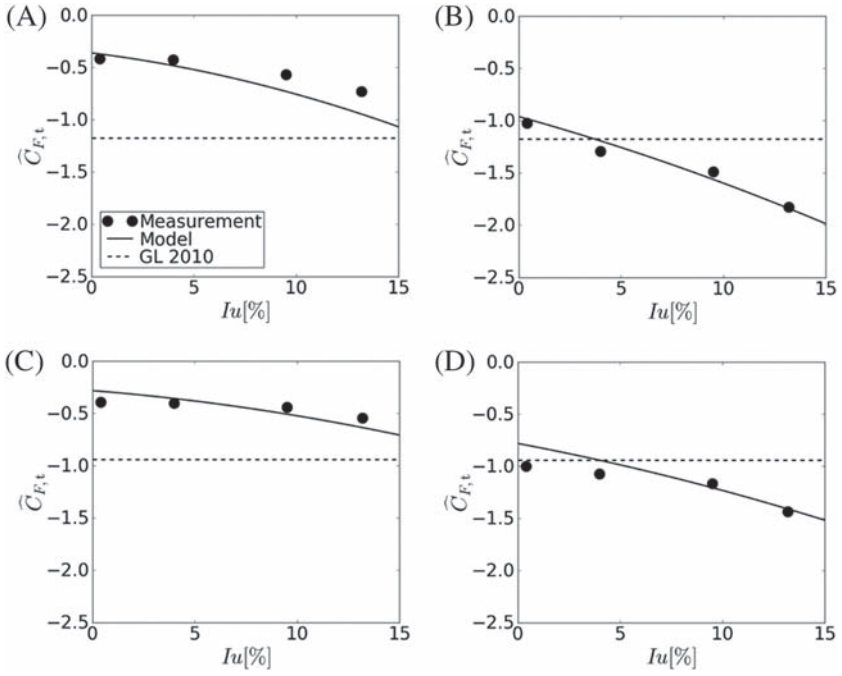

FIGURE 15 Peak force coefficient as a function of inflow turbulence intensity. A and B, Top surface of rectangular nacelle, C and D, Upper half of ellipsoidal nacelle. (A) and (C): for design load case (DLC) 6.1; (B) and (D): for DLC 6.2

$$C_{pi} = \begin{cases} -0.5 \text{ for } \widehat{C}_{pe} \geq 0 \\ 0.5 \text{ for } \widehat{C}_{pe} \leq 0. \end{cases} \tag{12}$$

Finally, the application of the proposed model to explain the damages of nacelle cover in Figure 1 is briefly discussed. It was reported that these damages were due to the peeling of adhesive between the nacelle cover (made of fiber-reinforced plastic [FRP]) and the steel frame during the typhoon.[12] Since the load on the cover during the typhoon exceeded the design strength of the FRP and the frame, it ultimately led to the deformation and the damage of the cover. To prevent similar accident in the future, nacelles were reinforced with an additional frame and FRP was changed from three layers 6 mm to seven layers 5 mm. In addition, the nacelle covers were fixed to the frame using bolts instead of simply using adhesive, and the effect of turbulence intensity was accounted for in the new nacelle cover design.

4 | CONCLUSIONS

The aerodynamics load experienced by two representative wind turbine nacelles—rectangular and ellipsoidal—under range of inflow turbulence conditions are investigated. Wind tunnel experiments are conducted to measure pressure field on the surface of the nacelle models for four different turbulence level and as a function of yaw misalignment. The conclusions of the study are summarized as follows:

1. The pressure distribution on the roof of the rectangular nacelle shows that the mean pressure coefficients for all four turbulence cases are similar for respective yaw angles. For the rectangular nacelle, $C_{p,\text{mean}}$ becomes more negative close to upstream edge with increasing inflow turbulence, though the downstream extent of such region reduces at the same time. For the ellipsoidal nacelle, a negative pressure field is generally observed on the downstream side of the nacelle surface due to an adverse pressure gradient. The magnitude of the mean pressure coefficient in the adverse pressure gradient region increases with decreasing inflow turbulence. The minimum $C_{p,\text{mean}}$ did not vary much with the inflow turbulence. This is particularly conspicuous for the upper surface.
2. Pressure data are integrated to compute the total vertical and sideways forces on the surfaces of two nacelles. It is observed that the peak forces acting on both rectangular and ellipsoidal nacelles increase with increasing inflow turbulence. For the case with turbulence inflow, the peak force coefficient for the rectangular nacelle occurs at a yaw misalignment of around 90°, while both vertical and sideways peak force coefficients are observed at a yaw misalignment of around 60° for the ellipsoidal nacelle.
3. The models for the estimation of the peak aerodynamic load are proposed based on analysis of the experimental data. The proposed models are a function of inflow turbulence and the mean force coefficient. The peak forces predicted by the model show good agreement with the measured values for both rectangular and ellipsoidal nacelles.
4. The predicted magnitude of the peak force coefficients by the GL guideline is larger than the measurements for DLC 6.1. However, the magnitude of the peak force coefficient predicted by the GL guideline for DLC 6.2 is lower than the measurements for the turbulence cases. When the inflow turbulence intensity is 13.2%, the GL guideline predicted values are 35% lower than the measured values for both nacelle shapes.

ACKNOWLEDGEMENTS

This research is carried out as part of Development of Advanced Wind Power Technology Project funded by ClassNK, Hitachi, Ltd, and Shimizu Corporation. The authors wish to express their deepest gratitude to the concerned parties for their support.

ORCID

Jay Prakash Goit https://orcid.org/0000-0002-2429-5259

REFERENCES

1. Robertson AN, Wendt F, Jonkman JM, et al. OC5 Project Phase II: Validation of global loads of the DeepCwind floating semisubmersible wind turbine. *Energy Procedia*. 2017;00:1-19.
2. Pahn T, Rolfes R, Jonkman J. Inverse load calculation procedure for offshore wind turbines and application to a 5-MW wind turbine support structure. *Wind Energy*. 2017;20:1171-1186.
3. Sessarego M, Ramos-García N, Sørensen JN, Shen WZ. Development of an aeroelastic code based on three-dimensional viscous–inviscid method for wind turbine computations. *Wind Energy*. 2017;20(7):1145-1170.
4. Rezaeiha A, Pereira R, Kotsonis M. Fluctuations of angle of attack and lift coefficient and the resultant fatigue loads for a large horizontal axis wind turbine. *Renew Energy*. 2017;114:904-916.
5. Storey RC, Norris SE, Cater JE. Modelling turbine loads during an extreme coherent gust using large eddy simulation. *J Phys: Conf Ser*. 2014;524:1-9.
6. Freebury G, Musial W. Determining equivalent damage loading for full-scale wind turbine blade fatigue tests. In: *19th ASME Wind Energy Symposium*, Reno, Nevada, USA; 2000:1-10.
7. White DL. New method for dual-axis fatigue testing of large wind turbine blades using resonance excitation and spectral loading. Tech. Rep. NREL/TP-500-35268, NREL, Colorado, USA; 2004.
8. Germanischer Lloyd. GL guideline for the certification of wind turbines.; 2010. http://www.gl-group.com.
9. IEC 61400-1. Wind energy generation systems - Part 1: Design requirements. Edition 4; 2019.
10. Ishihara T, Yamaguchi A, Takahara K, Mekaru T, Matsuura S. An analysis of damaged wind turbines by Typhoon Maemi in 2003. In: The Sixth Asia-Pacific Conference on Wind Engineering. ; 2005:1413-1428.
11. Wajima Wind Farm Number 2 Wind Turbine Nacelle Cover Damage Report; 2016. https://www.meti.go.jp/shingikai/sankoshin/hoan_shohi/denryoku_anzen/newenergy_hatsuden_wg/pdf/010_02_00.pdf. (In Japanese).
12. Minamiosumi Wind Farm Nacelle Cover Damage Report; 2017. https://www.meti.go.jp/shingikai/sankoshin/hoan_shohi/denryoku_anzen/newenergy_hatsuden_wg/pdf/012_04_00.pdf. (In Japanese).
13. Choi H, Jeon W-P, Kim J. Control of flow over a bluff body. *Annu Rev Fluid Mech*. 2008;40(1):113-139.
14. Chen X, Zhou N. Equivalent static wind loads on low-rise buildings based on full-scale pressure measurements. *Eng Struct*. 2007;29:2563-2575.
15. Tieleman HW. Wind tunnel simulation of wind loading on low-rise structures: a review. *J Wind Eng Ind Aerodyn*. 2003;91(12-15):1627-1649.
16. Tamura Y, Kareem A. Advanced Structural Wind Engineering. Springer; 2013.
17. Tamura Y, Suganuma S, Kikuchi H, Hibi K. Proper orthogonal decomposition of random wind pressure field. *J Fluids Struct*. 1999;13:1069-1095.
18. Holmes JD, Sankaran R, Kwok KCS, Syme MJ. Eigenvector modes of fluctuating pressures on low-rise building models. *J Wind Eng Ind Aerodyn*. 1997;69-71(1997):697-707.
19. Hiroshi N, Ishihara T. Wind tunnel test on mean wind forces and peak pressures acting on wind turbine nacelles. *Wind Energy*. 2014;17:1-17.
20. Goit JP, Liu Y, Ishihara T. Experimental study of wind load acting on wind turbine nacelles. In: *The Science of Making Torque from Wind Journal of Physics: Conf. Series 1037*. ; 2018:052019.
21. Liu Y, Goit JP, Ishihara T. Effect of turbulence intensities on pressure distribution of wind turbine nacelles in wind tunnel experiment. In: *Grand Renewable Energy*. Vol GRE2018. Pacifico Yokohama, Yokohama, Japan; 2018:O-We-7-5.
22. Zahle F, Sørensen NN. Characterization of the unsteady flow in the nacelle region of a modern wind turbine. *Wind Energy*. 2010;14:271-283.
23. Masson C, Smaïli A. Numerical study of turbulent flow around a wind turbine nacelle. *Wind Energy*. 2006;9(3):281-298.
24. Smaïli A, Masson C, Taleb SR, Lamarche L. Numerical study of thermal behavior of a wind turbine nacelle operating in a nordic climate. *Numer Heat Transf Part B Fundam*. 2006;50(2):121-141.
25. Holmes JD. *Wind Loading of Structures*. 3rd ed. CRC Presee Taylor & Francis Group; 2015.
26. Ishihara T. *Guidelines for Design of Wind Turbine Support Structures and Foundations*. Japan Society of Civil Engineers (JSCE); 2010 (In Japanese).

How to cite this article: Goit JP, Ishihara T. Aerodynamic loads on wind turbine nacelles under different inflow turbulence conditions. *Wind Energy*. 2020;23:645–659. https://doi.org/10.1002/we.2449